Journal of Materials Chemistry C

ROYAL SOCIETY OF CHEMISTRY

COMMUNICATION

View Article Online
View Journal | View Issue



Cite this: J. Mater. Chem. C, 2026, 14, 581

Received 3rd July 2025,
Accepted 25th November 2025

DOI: 10.1039/d5tc02554k

rsc.li/materials-c



# Solution-based synthesis of nanocrystalline $KBiS_2$ films at low temperatures and study of photoinduced charge generation

Marco Sigl, [a] Melissa Egger, [a] Daniel Knez, [b] Harald Fitzek, [c] Dmytro Neshchadin, [d] Ison Hau, [e] Thomas Webb, [e] Fernando Warchomicka, [f] Jiawen Han, [e] Ruiqi Wu, [e] Alex M. Ganose, [e] Georg Gescheidt, [d] Gerald Kothleitner, [b] Gregor Trimmel, [a] Saif A. Haque *[e] and Thomas Rath *[a]

**Ternary metal sulfides have been widely investigated in recent years as solar absorber materials in photocatalysis and photovoltaics, where they have the potential to replace expensive or harmful materials like noble metals or lead-based compounds. Potassium bismuth sulfide has two polymorphs showing promise for solar applications. However, the preparation of $KBiS_2$ is hardly investigated beyond the originally proposed highly energy demanding solid state or salt melt syntheses. In order to facilitate the applicability of $KBiS_2$ films, we investigated the formation of cubic and rhombohedral $KBiS_2$ from metal xanthate precursors. The use of xanthates offers the advantages of low conversion temperatures and good solubility of the precursors in non-halogenated and non-aromatic solvents. We successfully prepared $KBiS_2$ films with rhombohedral and cubic crystal structures, which we could confirm with XRD and HR-STEM experiments, and found that the cubic phase forms at a relatively low temperature of 200 °C. Our findings provide a facile low temperature method to prepare $KBiS_2$ thin films and demonstrate well-suited optoelectronic properties of this material. In particular, the long charge recombination lifetime of 41.1 microseconds in $TiO_2$/$KBiS_2$/spiro-OMeTAD films highlights the suitability of $KBiS_2$ for potential applications in solar energy conversion devices.**

## Introduction

With rising energy demands and the need to replace fossil fuels, solar energy is gaining increasing attention as a sustainable alternative. Materials with strong light absorption, suitable bandgaps, and low cost are essential for future applications in photovoltaics[1–4] and photocatalysis,[5–8] including solar fuel production and wastewater treatment. Recently, increasing interest has fallen onto metal chalcogenides, as they commonly show very suitable optical properties for solar energy conversion. A large group of metal chalcogenides are ternary metal sulfides, which combine two different metal cations and a sulfur anion to yield a plethora of structures. Ternary metal sulfides, such as $CuInS_2$, $Cu_3BiS_3$, $AgBiS_2$, $ZnIn_2S_4$ and $CuSbS_2$, typically show a bandgap in the visible range, making them promising candidates for utilization of sunlight.[4,9–13]

Bismuth sulfide itself is known to have high absorption coefficients and a low bandgap around 1.3 eV in the visible range.[14] Furthermore, introducing an additional metal ion to create ternary bismuth sulfides can lead to an improved charge carrier concentration.[15] Aluminum- or nickel-doped bismuth sulfides and ternary phases such as $CuBiS_2$, $Cu_3BiS_3$ and $AgBiS_2$ have been reported in photovoltaic or photocatalytic applications.[16–22]

An emerging and versatile ternary bismuth-based sulfide is potassium bismuth sulfide. Depending on the ratio of potassium to bismuth, several crystal structures, like orthorhombic,[23] rhombohedral[24] and cubic[24,25] crystal phases, are reported. The cubic $KBiS_2$ crystallizes in a simple rock salt structure ($Fm\bar{3}m$) and is reported with an optical bandgap of 1.61 eV.[4,26] While the properties of this material are very interesting, its synthesis typically involves high temperature processes. $KBiS_2$ is usually synthesized *via* solid state or salt melt syntheses using powdered Bi, $K_2CO_3$ and elemental sulfur at high temperatures of around 800 °C for several hours.[24,27] The $K_2S_5$ salt flux based synthesis of rhombohedral $KBiS_2$ reported by Qu *et al.* takes place at 600 °C for a prolonged time.[28] Even the $K_3BiS_3$ intermediate phases reported by McClain *et al.* still require 450 °C for 48 h.[24]

[a] Institute for Chemistry and Technology of Materials, NAWI Graz, Graz University of Technology, Stremayrgasse 9, 8010 Graz, Austria. E-mail: thomas.rath@tugraz.at
[b] Institute of Electron Microscopy and Nanoanalysis, Graz University of Technology, Steyrergasse 17, 8010 Graz, Austria
[c] Graz Centre for Electron Microscopy, Steyrergasse 17, 8010 Graz, Austria
[d] Institute of Physical and Theoretical Chemistry, Graz University of Technology, Stremayrgasse 9, 8010 Graz, Austria
[e] Department of Chemistry, Molecular Sciences Research Hub, Imperial College London, White City Campus, 82 Wood Lane, W12 0BZ London, UK. E-mail: s.a.haque@imperial.ac.uk
[f] Institute of Materials Science, Joining and Forming, Graz University of Technology, Kopernikusgasse 24, 8010 Graz, Austria

Recently, Yang *et al.* reported a successful hot-injection synthesis, using the long chained oleylamine and oleic acid. With this approach, they obtained nanocrystalline $KBiS_2$ at 250 °C. However, the obtained crystallites are very small (7.4 nm) and the remaining ligands at the surface can interfere with the optoelectronic properties. Nonetheless, the photodetectors manufactured with these nanoparticles proved to show an excellent photoresponse.[26] However, in order to utilize $KBiS_2$ as a broadly applicable semiconductor for solar energy conversion, a synthetic method yielding crystalline thin films at low temperature and short reaction times would be highly beneficial.

A promising approach to prepare $KBiS_2$ with lower energy demand is *via* the use of metal alkyl xanthates. Metal xanthates (also known as metal dithiocarbonates) are the metal salts of xanthogenic acid. They can act as single source precursors for the corresponding metal sulfides, meaning they are both metal and sulfur sources.[13,29–33] Metal xanthates can be easily prepared for most metals either using commercially available potassium xanthates as precursors or by preparing them directly from metal hydroxides or alkoxides. Additionally, metal alkyl xanthates are soluble in various solvents, depending on the used alkyl moiety. This enables a versatile method to prepare defined metal sulfide thin films from these precursors.[10,34–40]

In this study, we present a method to prepare rhombohedral and cubic potassium bismuth sulfide ($KBiS_2$) thin films from potassium and bismuth xanthates at significantly lower temperatures compared to the common solid-state approach (see Fig. S1). Using the ethyl xanthates of these metals offers good availability, as potassium ethyl xanthate is inexpensive and commercially available. The bismuth analogue can be synthesized *via* simple ligand exchange from potassium xanthate.[37] We investigated the crystal formation at different temperatures by X-ray diffraction and took a closer look at samples with different precursor ratios with HR-STEM. We performed first principles calculations to understand the fundamental optoelectronic behavior and band alignments. Moreover, we studied the optical and photochemical properties with reflectance-, electron paramagnetic resonance and transient absorption spectroscopy to obtain a deeper understanding of charge carrier generation and lifetime in $KBiS_2$ and heterojunctions with $TiO_2$ as well as p-type organic semiconductor contacts.

## Results and discussion

### Phase formation and structural characterization

For the preparation of $KBiS_2$ thin films, potassium ethyl xanthate (KXaEt) was recrystallized with acetone and methanol. In addition, bismuth ethyl xanthate ($Bi(XaEt)_3$) was synthesized from KXaEt and bismuth nitrate as previously reported,[37] and the synthesis is described in more detail in the Experimental section. To begin with, we investigated the thermal conversion of the potassium and bismuth xanthates as well as mixtures of both metal xanthate powders in K : Bi-molar ratios of 1 : 1, 1.5 : 1 and 2 : 1. The results of the thermogravimetric analyses (Fig. 1a) provide valuable insights; the decomposition temperature and rate can distinctly influence the properties of the formed metal sulfide. While $Bi(XaEt)_3$ shows a single sharp mass loss step at a relatively low temperature (5% mass loss) at 120 °C, KXaEt, in contrast, requires a notably higher temperature, exhibiting a sharp main mass loss with a decomposition onset at 210 °C, followed by a continuous mass loss. The main mass loss correlates with the decomposition of the organic side chains and the evaporation of the decomposition products. The

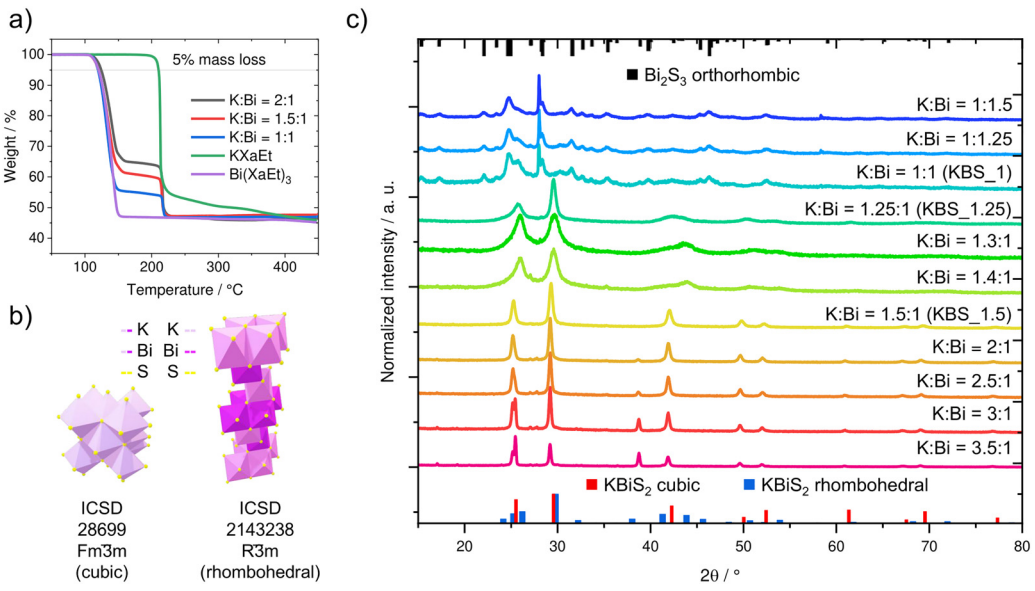


Fig. 1 (a) TGA curves with heating rates of 10° $min^{-1}$ of the individual KXaEt and $Bi(XaEt)_3$ precursors, as well as K : Bi mixtures with molar ratios of 1 : 1, 1.5 : 1 and 2 : 1; (b) crystal structures of cubic and rhombohedral $KBiS_2$ visualized with VESTA;[41] and (c) X-ray diffractograms of different mixtures of KXaEt and $Bi(XaEt)_3$ annealed at 300 °C for 30 min; the diffractograms are vertically shifted for better visibility with ICSD 28699 as the reference for cubic $KBiS_2$ in red bars,[25] ICSD 30775 as the reference for orthorhombic $Bi_2S_3$ in black bars[42] and ICSD 143475 as the reference for rhombohedral $KBiS_2$[24] in blue bars.

 

Table 1 Theoretical and experimental mass losses at 300 °C of the individual xanthate precursors, with different potassium sulfide compositions considered, and the respective mixtures with different K : Bi ratios, as well as the decomposition onset (temperature at 5% mass loss)

| | Theoretical mass loss/% | Experimental mass loss/% | Decomposition onset temperature/°C |
|---|---|---|---|
| KXaEt → $K_xS_y$[a] | 45.6–65.6[a] | 45.7 (250 °C)<br>49.6 (300 °C)<br>50.8 (350 °C) | 210.3 |
| $Bi(XaEt)_3$ → $Bi_2S_3$ | 55.1 | 53.7 | 120.3 |
| K : Bi = 1 : 1 | 57.4 | 55.4 | 120.4 |
| K : Bi = 1.5 : 1[b] | 55.8[b] | 54.6 | 120.6 |
| K : Bi = 2.0 : 1[b] | 54.8[b] | 53.7 | 121.7 |

[a] Expected mass loss between 45.6% ($K_2S_3$) and 65.6% ($K_2S$). [b] The excess of KXaEt was considered with 49.6% mass loss from the experimental KXaEt measurements (300 °C).

subsequent smaller ongoing loss of mass can be explained by the formation of different potassium sulfide phases with decreasing sulfur content at higher temperatures, as potassium xanthate forms a mixture of several phases (the diffractogram of a KXaEt film annealed at 300 °C for 30 min is shown in the SI, Fig. S2). In contrast to potassium xanthate, the mixtures of KXaEt and $Bi(XaEt)_3$ show no further mass loss after the characteristic 2-step decomposition.

The theoretical and experimental mass losses are summarized in Table 1. The experimental mass losses of the mixtures are only slightly lower than the theoretical ones. This is most likely caused by small amounts of carbon-based residues of the alkyl chains, which remain in the solid during the thermogravimetric analysis.

To fabricate the thin films (see scheme Fig. S1), we first prepared the individual precursor solutions with concentrations of 0.136 mmol $mL^{-1}$ in the non-halogenated solvents methanol and tetrahydrofuran (MeOH : THF 1 : 3, v : v). We subsequently mixed the precursor solutions in the volume ratios of the desired potassium to bismuth ratios.

As previous studies used an excess of potassium for the synthesis of $KBiS_2$,[24,27] we combined different K : Bi ratios ranging from K : Bi = 3.5 : 1 (potassium-rich) to 1 : 1.75 (bismuth-rich). We dropcast the solutions onto glass substrates and annealed them at 300 °C for 30 min under an $N_2$ atmosphere. The X-ray diffractograms of the samples with different ratios are depicted in Fig. 1c. In this experimental series, we found that a 1.5 times excess of the potassium precursor at an annealing temperature of 300 °C is optimal for the formation of cubic $KBiS_2$, which can be seen clearly in the diffractogram of the 1.5 : 1 sample in Fig. 1c. The diffraction pattern shows reflections matching with the ICSD 28699 reference, with the main ones at 25.5 (111), 29.6 (200) and 42.3° 2$\theta$ (220). No additional signals from impurities or secondary phases are observable.

The conditions used in the synthesis of $KBiS_2$ herein are remarkably less energy consuming than for the salt melt preparation found in the literature.[24,27] Moreover, our route results in materials with primary crystallite sizes (estimated *via* the Scherrer equation based on the XRD peak broadening, see Table S1) of approx. 15 nm. This is comparable with a reported hot-injection route, which is performed at a similar temperature, and leads to nanoparticles with diameters of approx. 13 nm.[26] At temperatures of 300 or 350 °C, the primary crystallite size of $KBiS_2$, prepared with the herein described approach based on metal xanthates, leads to primary crystallite sizes of approx. 22 and 29 nm, respectively.

For a stoichiometric K : Bi ratio or an excess of $Bi(XaEt)_3$, we exclusively observe the formation of orthorhombic $Bi_2S_3$ as a crystalline material (see Fig. 1c). For reference purposes, we prepared $Bi_2S_3$ films from only $Bi(XaEt)_3$ (SI, Fig. S3 and S4). As we do not observe a distinct crystalline potassium sulfide phase in the KBS_1 sample (K : Bi = 1 : 1), we expect the potassium precursor to form an amorphous potassium sulfide species, which may reside at grain boundaries or surfaces, explaining their absence in the diffraction data. This hypothesis is further examined by transmission electron microscopy (*vide infra*). It is also interesting to note that upon increasing the KXaEt amount to an excess of 1.25, we can see the formation of the rhombohedral $KBiS_2$ phase, which is corroborated by the peaks at 26.2 and 29.8° 2$\theta$ in the diffractogram, corresponding to the 012 and 104 reflections of rhombohedral $KBiS_2$, respectively. In the samples with an increasing amount of potassium xanthate from KBS_1.25 (K : Bi = 1.25 : 1) to KBS_1.5 (K : Bi = 1.5 : 1), we see a gradual change of the crystal structure, with only the cubic phase present in the KBS_1.5 sample (Fig. 1c).

A further increase of the potassium content (ratios from 2 : 1 to 3.5 : 1) in the precursor solution still led to the formation of cubic $KBiS_2$ as the main phase. In addition, as we do not observe any other potassium bismuth sulfide phases like $K_3BiS_3$, we expect increasing amounts of potassium-based phases to be formed in the increasingly potassium-rich samples. This is indicated, *e.g.*, by the emerging peaks at 17.1, 19.2, 25.2, 27.1 and 27.8° 2$\theta$ in the samples with a potassium excess of 2-fold and greater.

In addition to the investigation of different K : Bi ratios (Fig. 1c), we varied the annealing temperature for three different K : Bi ratios to get a better insight into the phase formation. In Fig. 2a (K : Bi = 1 : 1; KBS_1), we can see mostly the orthorhombic $Bi_2S_3$ phase, which becomes more crystalline with increasing temperature. Small amounts of the $KBiS_2$ phase are present up to 300 °C.

Although KBS_1.25 forms rhombohedral $KBiS_2$ at 300 °C, at lower temperatures (200 and 250 °C) the cubic phase seems to be preferred (Fig. 2b). The preferential formation of the cubic phase at lower temperatures indicates that this modification is kinetically favored under our synthesis conditions. While the underlying mechanism is not yet fully understood, it may be related to differences in nucleation and growth kinetics between the cubic and rhombohedral phases. While in the TGA (performed with a heating rate of 10° $min^{-1}$), the decomposition of potassium xanthate has barely started at 200 °C (*cf.* Fig. 1a), half an hour holding at 200 °C is sufficient to compensate for the lower temperature and obtain full

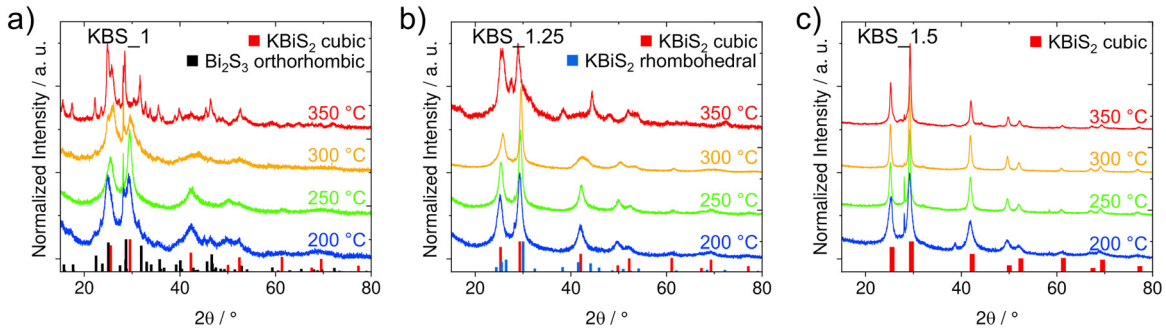


Fig. 2 X-ray diffractograms of samples prepared from the following K : Bi mixtures at different temperatures between 200 and 350 °C: (a) 1 : 1 (KBS_1), (b) 1.25 : 1 (KBS_1.25) and (c) 1.5 : 1 (KBS_1.5). The diffractograms are vertically shifted for better visibility with ICSD 28699 as the reference for cubic $KBiS_2$ in red bars,[25] ICSD 30775 as the reference for orthorhombic $Bi_2S_3$ in black bars[42] and ICSD 143475 as the reference for rhombohedral $KBiS_2$[24] in blue bars.

conversion of the xanthates to the metal sulfides as depicted in Fig. S5. At 350 °C, the orthorhombic $Bi_2S_3$ is again the most prominent phase also in the KBS_1.25 sample series. In comparison, the 1.5-fold potassium excess in KBS_1.5 results in cubic $KBiS_2$ at all four temperatures (Fig. 2c). With increasing temperature, the crystallinity increases as well and primary crystallite sizes from 10 ± 2 (200 °C) up to 29 ± 7 nm (350 °C) are estimated using the Scherrer equation (see also Table S1). At 200 and 250 °C, we observe a small additional sharp peak at 28.1° 2$\theta$, which hints at a $Bi_2S_3$ secondary phase. Upon increasing the temperature to 300 °C, we only see signals corresponding to cubic $KBiS_2$. However, above 300 °C, a secondary unidentified phase emerges with minor peaks at 27.4°, 38.3° and 44.5° 2$\theta$. These peaks match well with the phase, which we also observe in samples with a higher potassium excess (*e.g.*, K : Bi = 2 : 1; Fig. 1c), where starting at a 2-fold potassium excess, additional small peaks emerge (*vide supra*).

Next, we performed Raman spectroscopy measurements on the samples with different K : Bi ratios (Fig. S6, SI). The spectrum of KBS_1 matches spectra found in the literature for $Bi_2S_3$,[43,44] with a broad amorphous background, which we assign to the remaining potassium sulfide. The reported bands below 100 $cm^{-1}$ could not be resolved in this measurement, due to the cut-off filter at 70 $cm^{-1}$. Due to the strong amorphous background, the bands between 200 and 300 $cm^{-1}$ could not be resolved individually. With increasing potassium content, these bands decrease in intensity and are not present in the KBS_1.5 sample. At the same time, the broad peak around 190 $cm^{-1}$ and the shoulder between 200 and 350 $cm^{-1}$ shift to higher wavenumbers, indicating an exchange of the heavy bismuth with lighter potassium atoms, matching well with the formation of the potassium bismuth mixed phase.

This change from the individual binary phases, present in the KBS_1 sample, to the ternary $KBiS_2$ phases, present in the KBS_1.25 and KBS_1.5 samples, is additionally confirmed by the STEM-HAADF images, where we clearly observe the formation of large crystalline bismuth sulfide needles and amorphous potassium sulfide regions for KBS_1 (Fig. 3). HR-STEM images combined with multislice simulations confirm the orthorhombic $Bi_2S_3$ crystal phase of the needles that grow up to hundreds of nm in length (Fig. 4a and Fig. S7). With a higher

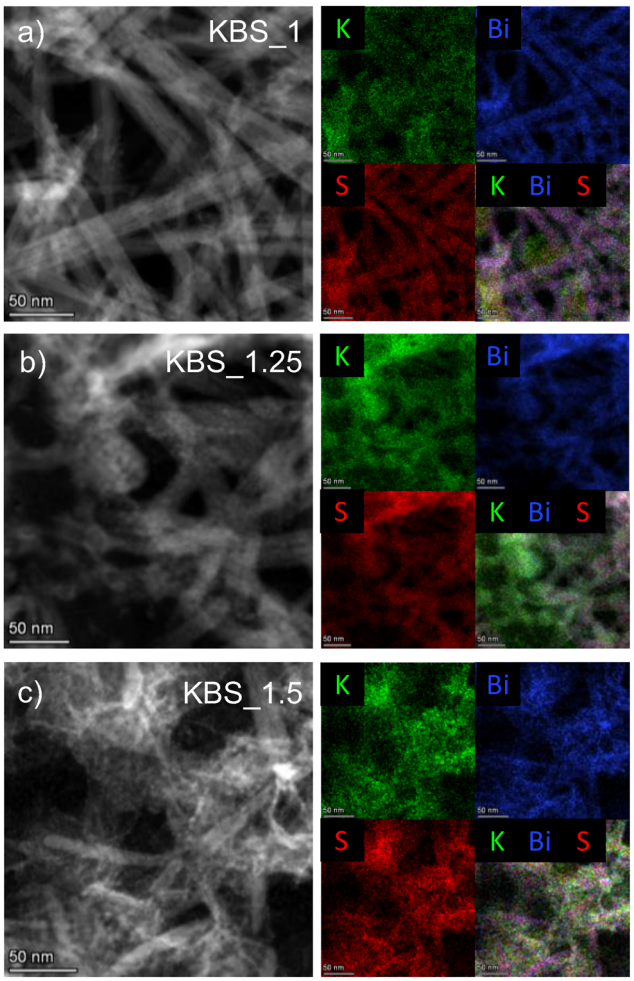


Fig. 3 STEM-HAADF micrographs (left) and corresponding EDX elemental maps (right) of (a) KBS_1, (b) KBS_1.25 and (c) KBS_1.5, with K in green, Bi in blue and S in red.

potassium content, potassium and bismuth mixed regions with still amorphous potassium sulfide regions in between are revealed in KBS_1.25 (Fig. 3b). In the KBS_1.5 sample, we see that K and Bi are intermixed well in the elemental mapping (Fig. 3c). Moreover, we can still observe needle-like structures in

 

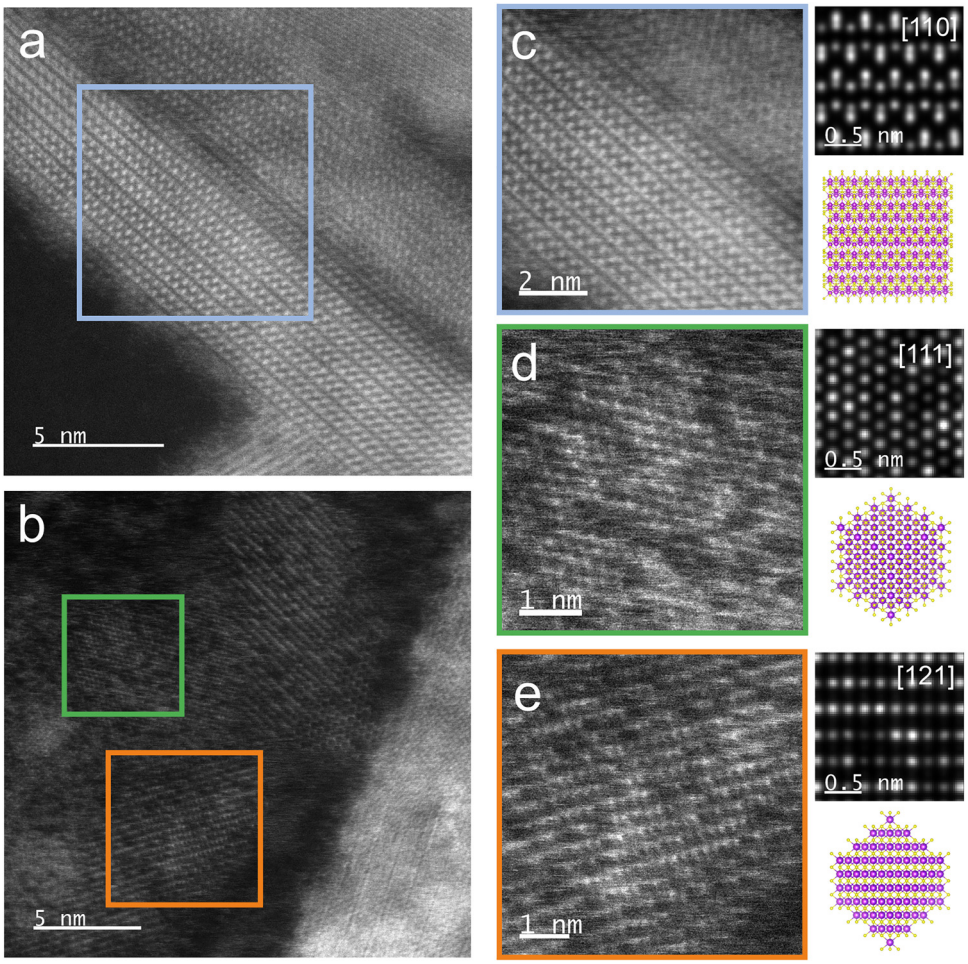


Fig. 4 HR-STEM-HAADF images of (a) KBS_1 and (b) KBS_1.5; (c) $Bi_2S_3$ oriented in the 110 plane direction with a multislice simulation and a ball-stick visualization of the reference structure in VESTA;[41] (d) cubic $KBiS_2$[25] oriented in the [111] direction and (e) in the [121] direction with corresponding multislice simulations[45] and ball-stick visualizations.

KBS_1.25 and KBS_1.5; however, with the increased potassium content, the growth of the needles is inhibited as seen in the STEM images and elemental maps (Fig. 3 and Fig. S8).

High-resolution STEM-HAADF images (Fig. 4b) further reveal the nanocrystalline morphology of the cubic $KBiS_2$ phase in the KBS_1.5 sample. Several $KBiS_2$ crystallites with a size of $<10$ nm are visible in the presented image, two of which are found to be oriented in the [111] (green box) and [121] (orange box) crystallographic orientation. A comparison with multislice simulations confirms a match to the cubic $KBiS_2$ phase. The HR-STEM images in Fig. 4d and e additionally show the random alternation of the potassium and bismuth atoms at the metal sites in the cubic crystal lattice, appearing in different brightness due to the large difference in atomic number of the two elements. These contrast variations are closely mirrored in the corresponding multislice simulations of cubic $KBiS_2$, assuming random occupation of K and Bi in the underlying model structure.

### Optical properties and first principles simulations

We investigated the optical properties of the $KBiS_2$ films using diffuse reflectance and transmission measurements. We note that due to the macro-porosity of all films as revealed by the SEM investigations (Fig. S9), the determined absorption coefficients of these samples ($>2.10^4$ $cm^{-1}$ below approx. 600 nm; Fig. S10a) are lower than they would be for a dense film. To characterize the optical bandgaps of the materials, we used the Kubelka–Munk[46] method and corresponding Tauc plots[47] with the support of density functional theory simulations. The absorption spectra, Kubelka–Munk and Tauc plots are depicted in Fig. S10b and c and the corresponding reflectance spectra are shown in Fig. S11.

In all three samples, we found indirect and direct transitions, which have been reported in the literature for metal sulfides before.[48] The direct contributions are much more pronounced and at slightly higher energies than the indirect ones. Interestingly, in the KBS_1 sample, the indirect contribution is much stronger than the one in the pure $Bi_2S_3$ film and of marginally lower energy with 1.04 eV in the mixture compared to 1.10 eV in the pure $Bi_2S_3$ film (Fig. S12). This might be associated with the incorporation of $K^+$ on $Bi^{3+}$ sites, which can induce lattice expansion and local strain and could thereby influence the band structure, leading to a red shift in optical

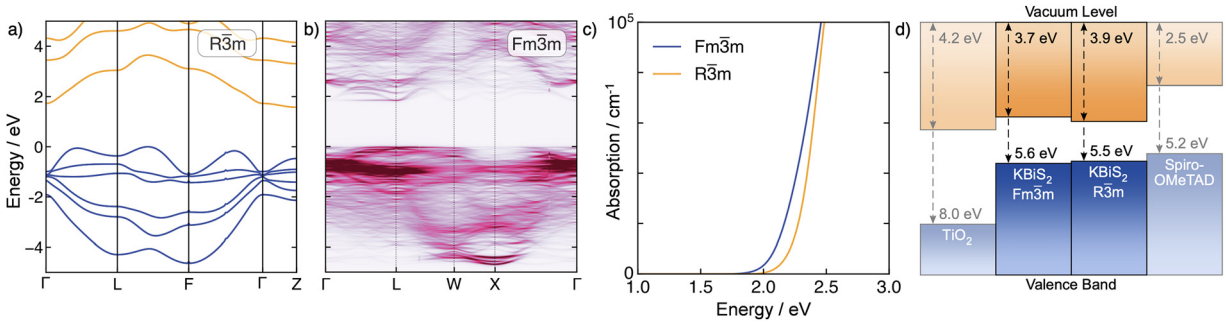


Fig. 5 Optoelectronic properties of $KBiS_2$ calculated using the HSE06 + SOC functional. Electronic band structure of $KBiS_2$ in the (a) rhombohedral and (b) cubic structures. (c) Calculated optical absorption and (d) band alignment against electron and hole contact materials. The ionization potential and electron affinity for $TiO_2$ and spiro-OMeTAD were taken from the study of Jena *et al.*[52]

absorption. A similar band gap energy reduction was reported by Silva *et al.*, who investigated the substantial influence of iron doping on the indirect bandgap of $Bi_2S_3$.[49] The optical bandgaps of $KBiS_2$ correspond well to previously reported values. For example, the direct transition of 1.80 eV for the cubic thin film is only slightly higher than the value reported in the literature (1.61 eV) and the indirect bandgap of 1.29 eV of the rhombohedral $KBiS_2$ thin film is well comparable to the value of 1.21 eV from the literature. The experimental optical bandgaps are summarized in Table S2 with corresponding values from the literature. Due to the nanocrystalline nature of the metal sulfides resulting from xanthate precursors, the bandgaps are slightly higher.[14,50] The slightly increased bandgap observed for $KBiS_2$ may arise not only from quantum confinement effects due to the nanocrystalline domain size, but also from the presence of point defects. In particular, sulfur vacancies or antisite defects can locally modify the electronic structure and shift the absorption onset. The formation of such defects is plausible under the mild decomposition conditions of the metal xanthate precursors, where a marginally sulfur-deficient environment may occur. Consequently, both nanocrystallinity and defect-related electronic states are likely to contribute to the optical properties of the material.

Additionally, we performed density functional theory simulations using the hybrid HSE06 functional with the addition of spin–orbit coupling. The full computational methodology is provided in the Experimental section. The band structures of the rhombohedral and cubic structures are displayed in Fig. 5a and b, respectively. We find that the rhombohedral structure exhibits an indirect band gap of 1.58 eV. While our calculated band gap is ~0.3 eV larger than the indirect gap measured in experiments, this could be due to the lack of thermal effects in our calculations or the presence of defect states and disorder in thin film samples. The direct gap is ~0.5 eV larger than the indirect gap at an energy of 2.04 eV. This relatively strong indirect character is expected to result in reduced light absorption and weaker photovoltaic performance.

In contrast, the cubic structure displays a fundamental direct gap of 1.84 eV, in excellent agreement with the experimental value of 1.80 eV. For the cubic structure, we explicitly model a supercell with configurational disorder on the K and Bi sites and have therefore performed band unfolding to map the band structure back onto the primitive cell symmetry. We note that spin–orbit coupling plays a large role in governing the electronic properties and results in band gap renormalization of 0.23 and 0.56 eV for the cubic and rhombohedral structures, respectively.

The calculated effective masses are provided in Table 2. In the rhombohedral structure, electron and hole transport are expected to be highly anisotropic, with the effective masses in the $a/b$ directions over 4 times smaller than that in the $c$ direction (across the K/Bi layers). Electrons have significantly smaller effective masses of 0.21 $m_0$, which is comparable to those of other emerging chalcogenide absorbers such as $Sb_2Se_3$ (0.35 $m_0$[51]). The composition disorder in cubic-structured $KBiS_2$ provides fully isotropic transport but comes at the cost of secondary flat bands at the conduction and valence band edges. This results in both light and heavy electrons and holes contributing to transport. Similarly to the rhombohedral structure, the electron mobility is expected to be greater than the hole mobility due to the much smaller light effective masses (0.22 *vs.* 0.91 $m_0$). The calculated optical absorption displayed in Fig. 5c highlights the strong onset of absorption for both compounds; however, we note that these absorption spectrum simulations

Table 2 Calculated band gaps, electron $(m_e^*)$ and hole $(m_h^*)$ effective masses, ionization potentials (IP), and electron affinities (EA) of cubic- and rhombohedral-structured KBS obtained using hybrid density functional theory

| | Band gap/eV | | $m_e^*/m_0$ | | $m_h^*/m_0$ | | | |
|---|---|---|---|---|---|---|---|---|
| | Direct | Indirect | $a/b$ | $c$ | $a/b$ | $c$ | IP/eV | EA/eV |
| Rhombohedral | 2.04 | 1.58 | 0.21 | 2.51 | 0.88 | 4.12 | 5.51 | 3.92 |
| Cubic | 1.84 | — | 0.22, 3.15 | — | 0.91, 5.12 | — | 5.59 | 3.74 |

 

do not account for indirect optical transitions (due to the absence of temperature, 0 K) and therefore only reflect the direct band gap transitions in the rhombohedral structure. Finally, we obtained the predicted bulk band alignment through *ab initio* slab-vacuum models. The ionization potentials (IP) of both compounds were found to be 5.5–5.6 eV, while the electron affinities (EA) are 3.7–3.9 eV (Fig. 5d). Given how close these are to the band alignments of $MAPbI_3$ (IP = 5.5, EA = 3.9), it is expected that $KBiS_2$ devices can make use of the same electron and hole contact materials used in perovskite photovoltaics.

### Photoinduced oxygen radical formation and charge photogeneration in $KBiS_2$ films

For a qualitative assessment of the oxygen radical formation upon illumination, which is an important measure for photocatalytic activity, we performed EPR measurements using DMPO as a spin trap. The samples differ only in signal-to-noise ratio, but all show EPR spectra corresponding to a DMPO–$OH^{\bullet}$ adduct (Fig. S13, $a_N$ = 14.3 G, $a_H$ = 14.3 G).[53] The slight asymmetry observed in the EPR signals and minor alteration of the line intensities suggest the presence of a second radical species, most likely DMPO–$OOH^{\bullet}$.[54,55] This indicates that KBS_1, KBS_1.25 and KBS_1.5 generate oxygen centered free radicals upon light irradiation. Based on the literature, it is plausible that the initially formed DMPO–$OOH^{\bullet}$ adduct undergoes conversion to DMPO–$OH^{\bullet}$ within the time frame of our experimental setup (Scheme S1).[56–59] The absence of any signal without the presence of oxygen further suggests oxygen as a critical component for the formation of radicals.

We next considered light-induced charge generation, separation and recombination reactions. Fig. 6a presents the charge transfer processes occurring in $TiO_2$/KBS/spiro-OMeTAD films (KBS = $KBiS_2$) in which the KBS film (cubic phase, KBS_1.5) forms a heterojunction with the n-type $TiO_2$ and with the p-type spiro-OMeTAD. SEM images of such films are shown in Fig. S14 and the absorbance spectra are shown in Fig. S15. Light absorption by KBS is followed by electron transfer from KBS to $TiO_2$ and hole transfer from KBS to the spiro-OMeTAD hole transporting layer. High-yield and long-lived charge separation across the $TiO_2$/KBS/spiro-OMeTAD double heterojunction is a prerequisite for the successful exploitation of such layers in solar energy conversion devices (*e.g.*, photovoltaics or photocatalysis). Herein, we used transient absorption spectroscopy[60] to directly probe the hole transfer from KBS to spiro-OMeTAD (process 3, Fig. 6a) and the charge recombination kinetics (process 6, Fig. 6a). Full details of the used transient absorption spectrometer are provided in the Experimental section. We note that for the transient optical studies, we used sample KBS_1.5 owing to the higher crystallinity and less sensitive preparation of the cubic $KBiS_2$.

We determined the kinetics of charge recombination between the photogenerated electrons in $TiO_2$ and holes in spiro-OMeTAD (process 6, Fig. 6a) by monitoring the decay of the $[spiro\text{-}OMeTAD]^+$ polarons at 1600 nm following pulsed excitation at 510 nm. Typical decay dynamics of different heterojunctions are presented in Fig. 6b. We note that no transient absorption signal is observed in the pristine KBS sample, indicating that electron–hole recombination dynamics in KBS occurs on timescales faster than the instrument response of our transient spectrometer (IRF = 100 ns).

With respect to the Beer–Lambert law, the change in optical density (ΔOD) is related to the concentration of photogenerated $[spiro\text{-}OMeTAD]^+$ and is therefore a measure of the yield of hole transfer. Fig. 6c presents $m\Delta OD_{max}$ (defined as ΔOD at 1 μs) values for the samples investigated herein. Taken together, these data indicate the importance of the $TiO_2$ electron acceptor in achieving a high yield of hole transfer. We fitted the transient absorption kinetics in Fig. 6b with a stretched exponential function: $\Delta OD \propto \exp[-(t/t_0)^{\alpha}]$ (details are provided in the Experimental section and Table S3). Given the multiexponential nature of the kinetic traces, we define a charge recombination lifetime, $\tau_{CR}$, as the time taken for ΔOD to reach 50% of its initial value. In this way, we estimate $\tau_{CR}$ = 41.1 μs in $TiO_2$/KBS/spiro-OMeTAD films reported herein. It is pertinent to

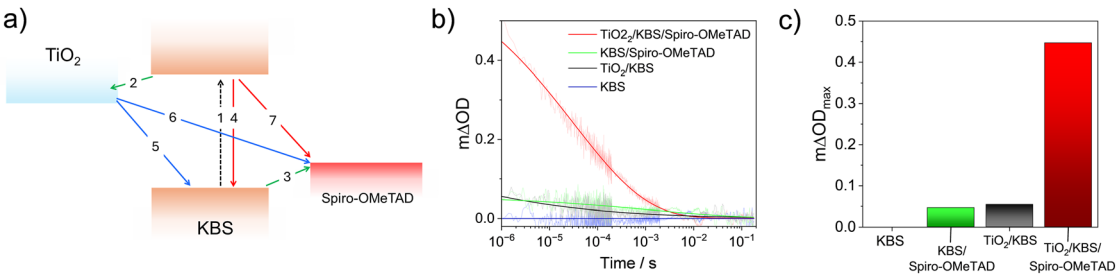


Fig. 6 (a) Diagram depicting the charge separation (green arrows) and recombination (red and blue arrows) processes in the $TiO_2$/KBS/spiro-OMeTAD double heterojunction, where KBS = $KBiS_2$. Light absorption by KBS leads to photoexcitation of an electron (process 1). Charge separation occurs *via* transfer of the photoexcited electron in KBS to the conduction band of $TiO_2$ (process 2) and extraction of the corresponding hole in KBS to spiro-OMeTAD (process 3). Competing with the charge separation process is the relaxation of the photoexcited electron in KBS (process 4) as well as interfacial charge recombination of electrons in $TiO_2$ with either holes in the KBS layer (process 5) or the spiro-OMeTAD HTM (process 6). An additional reaction involves recombination of electrons in KBS and holes in spiro-OMeTAD (process 7). (b) Time-resolved transient absorption measured at 1600 nm for mp-$TiO_2$/KBS/spiro-OMeTAD (red), KBS/spiro-OMeTAD (green), mp-$TiO_2$/KBS (black) and pristine KBS (blue) films. (c) Bar chart showing relative yield of long-lived charge separation in the different films studied in b. $m\Delta OD_{max}$ is taken as the magnitude of the transient absorption signal 1 μs after pulsed laser excitation.

note that the $m\Delta OD_{max}$ and $\tau_{CR}$ values observed in our $TiO_2$/KBS/spiro-OMeTAD films are similar in magnitude to those reported in high-performing materials such as lead halide perovskite-based films.[61–63] This highlights the potential of KBS as a light harvesting material for future applications in solar energy conversion.

## Conclusion

In this study, we prepared potassium bismuth sulfide films with rhombohedral and cubic crystal phases and investigated their structural, optical and charge-generation properties. We could access both phases by adjusting the ratio of the xanthate precursors in a non-halogenated solvent mixture. Moreover, we investigated the formation of the phases and the influence of the precursor ratio, where an X-ray diffraction study revealed that cubic $KBiS_2$ already forms at 200 °C from a metal xanthate precursor film containing a 1.5-fold potassium excess. In cubic $KBiS_2$, K and Bi ions randomly occupy the metal sites of the cubic rocksalt structure, which we could directly observe in high resolution STEM images. We additionally discovered that with a smaller excess of potassium (K : Bi = 1.25 : 1) at an annealing temperature of 300 °C, the rhombohedral $KBiS_2$ phase can be obtained.

First principle simulations revealed a fundamental direct transition of 1.84 eV for cubic $KBiS_2$, matching well with the experimentally determined value. Furthermore, we investigated the charge generation and lifetime properties under illumination. EPR spectroscopy confirmed oxygen centered radicals in all investigated films and with additional transient absorption spectroscopy measurements, we could disclose an excellent charge carrier lifetime of 41.1 μs for cubic $KBiS_2$, when combined with suitable electron and hole transport layers, like $TiO_2$ and spiro-OMeTAD. Such a charge carrier lifetime is comparable to that of the high performing lead halide perovskites and shows the great potential of this material for solar applications.

Therefore, we will exploit this low temperature $KBiS_2$ thin film preparation method in future detailed investigations of the material as a solar absorber in photovoltaic devices and photocatalysis. In particular, we are convinced that in addition to the well-suited optical properties, the highly porous nature and the specific nanostructure of the films, as revealed by electron microscopic investigations, will be highly beneficial for the photocatalytic performance, allowing for a large available surface area and a facile diffusion of larger organic molecules towards and away from active sites.

## Experimental

**Chemicals.** The chemicals and solvents were purchased from commercial suppliers and used without further purification, except for potassium ethyl xanthate (potassium O-ethylcarbonodithioate, Sigma Aldrich), which was recrystallized from acetone/diethyl ether. The used chemicals and suppliers are given below: hydrochloric acid (37%, Fisher Scientific), absolute ethanol (Sigma Aldrich, ≥99.8%), acetone (p.a., Merck), diethyl ether (Sigma Aldrich, 99.5%), $Bi(NO_3)_3{\cdot}5H_2O$ (Sigma Aldrich, 98%), chloroform (Fisher Scientific, 99.8%), tetrahydrofuran (VWR, 99%), methanol (Normapur), anhydrous chlorobenzene (Sigma Aldrich), LiTFSI (Sigma Aldrich, 99.9%), FK209 (Sigma Aldrich), anhydrous acetonitrile (Acros, ≥99.9%), 4-*tert*-butylpyridine (Sigma Aldrich, 98%), and spiro-OMeTAD (Osilla, >99%).

**Synthesis of bismuth ethyl xanthate.** Potassium ethyl xanthate (KXaEt) was purchased from Sigma Aldrich and recrystallized from acetone and diethyl ether. Starting with the recrystallized potassium ethyl xanthate, the bismuth ethyl xanthate ($Bi(XaEt)_3$) was synthesized *via* ligand exchange according to the literature.[37] One equivalent of $Bi(NO_3)_3{\cdot}5H_2O$ was suspended in water and $HCl_{conc.}$ was added until it formed a clear solution (about 2.5 mL $mmol^{-1}$ of $Bi(NO_3)_3{\cdot}5H_2O$). An aqueous solution of potassium ethyl xanthate (3 equiv.) was added and the mixture was stirred for 30 min at room temperature. The yellow precipitate was collected by filtration and recrystallized from a hot chloroform solution. Yield: 45.8%.

$^1H$ NMR (300 MHz, $CDCl_3$): $\delta$ = 4.73 (q, 2H, $OCH_2$), 1.52 (t, 3H, $CH_3$) ppm.

**Preparation of $KBiS_2$ films.** The glass substrates were cleaned with deionized $H_2O$ and a dust-free tissue. Afterwards, they were treated in a 2-propanol bath in an ultrasonic bath for a few minutes and finally etched with an $O_2$ plasma (FEMTO, Diener Electronic) for 3 min. Stock solutions of KXaEt and $Bi(XaEt)_3$ with concentrations of 0.14 mmol in a MeOH : THF solvent mixture (1 : 3 v : v) were prepared and mixed in the desired precursor ratios. For the thin films, about 50 μL $cm^{-2}$ was pipetted on the substrate and spin coated (1500 rpm, 1500 rpm/s, 30 s) in air, resulting in films of approx. 80 nm thickness. For the thicker films (for X-ray diffraction), the same solutions were drop-coated, yielding film thicknesses of 6–10 μm. All samples were thermally annealed in the glovebox under an $N_2$ atmosphere.

**Preparation of the mp-$TiO_2$ films.** Titania paste was mixed with terpineol (1 : 1.5 weight ratio) and stirred overnight. The glass substrates were cleaned first with water and then with 2-propanol in an ultrasonic bath. The cleaned substrates were treated with oxygen plasma (Femto plasma etcher from Diener Electronic) for 3 min. The substrates were covered with the titania/terpineol mixture and spin coated (WS-650MZ-23NPPB) at 3000 rpm (ramp: 1000 rpm/s) for 50 s. The layers were dried at 80 °C for 15 min and annealed at 500 °C for 1 h to obtain mesoporous mp-$TiO_2$ films with a thickness of 1 μm. For the preparation of $KBiS_2$ films on mp-$TiO_2$, the above-described method was used.

## Characterization methods

**Thermogravimetry.** Thermogravimetric investigations were carried out with a PerkinElmer TGA8000.

**X-ray diffraction.** Thin film X-ray diffractograms were recorded with a Rigaku Miniflex 600 with a D/Tex Ultra detector using CuKα radiation and the evaluation of the diffraction patterns was performed with the SmartLabStudioII software.

**Crystal structures.** The crystal structures of $KBiS_2$ were visualized with the visualization program VESTA (v. 3.5.8.).[41]

**Film thickness.** The film thicknesses were measured with a DektakXT Profilometer from Bruker.

 

**SEM.** Scanning electron microscopy was performed with a TESCAN MIRA3 field emission scanning electron microscope (FESEM) using an in-beam secondary electron detector. The device was operated at 5 kV. The samples were coated with a 10 nm chromium layer by thermal evaporation. EDX spectra were recorded with an Octane Super detector from AMETEK EDAX at an energy of 15 kV.

**STEM.** High-resolution HAADF STEM investigations were carried out on a probe-corrected FEI Titan3 (Thermo Fisher Scientific, Eindhoven) operated at 300 kV with a field emission source (X-FEG) at a convergence angle of 19.6 mrad. The microscope is equipped with an electron energy-loss filter (GIF Quantum, Gatan) and a Super-X EDS detector (Thermo Fisher, Eindhoven). For the sample preparation, 10 μL of the precursor solutions used for the thin film preparation, with half the concentration, was put onto a Ni TEM grid (Ted Pella, Inc., Prod. No. 01824N), coated with a $<3$ nm amorphous carbon film and spin coated at 1500 rpm (ramp: 1500 rpm/s) for 30 s.

The STEM-HAADF images were simulated with the Dr Probe Multislice simulation package (developed by Juri Barthel at Forschungszentrum Jülich/Germany).[45] The full-width at half maximum of the probe was set to 0.08 nm. Crystallographic visualizations were rendered in VESTA (v. 3.5.8.).[41] EDX maps were acquired and analyzed in Velox by Thermo Fisher Scientific.

Due to the strongly $Z$ dependent scattering cross-section ($\sim Z^2$, with $Z$ being the atomic number), the HAADF contrast is dominated by the Bi atoms in the crystal, while the other constituents (K and S) remain almost invisible. For the simulations presented in Fig. 5, a 6 nm-thick crystal was generated. For $KBiS_2$, the Bi and K sites were randomly occupied.[25] The resulting contrast variations between individual atomic columns closely resemble those observed in the experimental data.

**Raman spectroscopy.** The samples, which were sealed under a nitrogen atmosphere, were opened and immediately transferred into an argon-filled glovebox (MBraun), where they were prepared on a SEM stub (fixed with C-tape) for subsequent analysis in the correlative SEM-Raman microscope (Zeiss Sigma 300 with WITec RISE system). To ensure oxygen-free transport from the glovebox, the samples were transferred to the high-resolution SEM in the Leica EM VCT500 transfer system. The Raman microscope (WITec RISE) is fully integrated in the vacuum chamber of the SEM and all measurements were performed in vacuum, using a laser wavelength of 532 nm and a Zeiss LD EC Epiplan-Noefluar 100×/0.75(NA) objective. To minimize sample damage by the laser, all samples were cooled to 208.15 K (−65 °C), using a Leica cryo stage and a laser power of only 0.3 mW was used. This low laser power made a long integration time of 120 seconds per spectrum necessary. To further improve the SNR, spectra from at least three positions on the surface were averaged and all spectra were background corrected using the WiTec 5.2 software.

**Optical characterization.** The absorption and reflectance spectra were recorded with a Shimadzu UV-2600i with an ISR-2600Plus integrating sphere. The absorbance of the films was calculated from the recorded diffuse reflectance and transmission spectra and converted to the absorption coefficient *via* the film thickness.

**EPR spectroscopy.** DMPO (5,5-dimethyl-1-pyrroline *N*-oxide) was used as the spin trap. The spin-trap solution (200 mM, 100 μl) was put on the surface of the spin-coated glass and distributed evenly. The samples were irradiated for 600 seconds using a high-intensity LED photoreactor operating at 405 nm. After the irradiation, the solution was collected from the glass surface. EPR spectra were recorded at room temperature using a MiniScope MS300 X-band EPR spectrometer (Magnetech). The time between irradiation and completion of EPR spectrum acquisition was approximately 10 minutes.

**First principles calculations.** Density functional theory calculations were performed using the Vienna *Ab initio* Simulation Package (VASP) utilising a plane wave basis set and the projector augmented wave (PAW)[64] method to describe the interactions between core and valence electrons. The hybrid Heyd–Scuseria–Ernzerhof (HSE06)[65,66] exchange–correlation functional was used for all structural relaxations. The geometric positions were relaxed until all forces totalled less than 0.01 eV $Å^{-1}$. Electronic band structures, optical properties, and band alignments were performed with the addition of spin–orbit coupling (SOC), which is known to be essential for systems containing heavy elements such as Bi. The icet package[67] was used to generate a special quasirandom structure[68] to model the disordered cubic structure. The resulting supercell was a non-diagonal expansion (matrix = [[−1, 0, −1], [−2, 0, 2], [−1, 4, −1]]) of the face-centred-cubic primitive cell structure and contained 32 atoms. A plane wave energy cutoff of 500 eV was found to converge the total energy to less than 5 meV $atom^{-1}$. $2 \times 2 \times 2$ and $4 \times 4 \times 4$ Γ-centred $k$-point meshes were found to converge the total energy to 1 meV $atom^{-1}$ for the cubic supercell and rhombohedral primitive cell, respectively. Band structures were plotted using the sumo[69] and easyunfold[70] packages. Band alignments were obtained using the slab-vacuum approach, with a 30 Å slab and 30 Å vacuum generated using the surfaxe package[71] and the plots generated using the bapt package (https://github.com/utf/bapt/tree/master).

**TAS.** $TiO_2/KBiS_2$/spiro-OMeTAD samples were prepared by spin coating a spiro-OMeTAD layer on $TiO_2$/KBS substrates using a spin speed of 4000 rpm for 20 s. The spiro-OMeTAD solution was prepared using 90 mg of spiro-OMeTAD dissolved in 1 ml of anhydrous chlorobenzene and doped with 24 μL LiTFSI solution (520 mg $mL^{-1}$) and 10 μL FK209 (300 mg $mL^{-1}$) solution both dissolved in anhydrous acetonitrile and 40 μL 4-*tert*-butylpyridine. Samples for microsecond transient absorption spectroscopy (TAS) measurements were stored in a nitrogen-filled glovebox and taken in a sealed quartz cuvette for measurement. The $TiO_2/KBiS_2$/spiro-OMeTAD films were excited by a Nd:YAG laser (Opolette UX tunable OPO laser, nanosecond pulse width). A 100 W quartz halogen lamp (Bentham IL1) was used as the probe source. The probe wavelength was adjusted using a monochromator and set to 1600 nm. This probing beam was detected using an InGaAs photodiode (Hamamatsu Photonics) before being filtered and amplified (Costronics Electronics) and finally interpreted by a digital oscilloscope (Tektronics DPO3012). All TAS measurements were conducted employing 510 nm laser pulses (150 μJ $cm^{-2}$).

## Author contributions

M. S: conceptualization, data curation, formal analysis, synthesis and investigation, characterization methodology, project administration, visualization, writing – original draft, and writing – review & editing; M. E.: conceptualization, data curation, investigation, and writing – review & editing; D. K.: investigation, data curation, and review & editing; H. F.: conceptualization, investigation, data curation, and review & editing; D. M.: investigation, data curation, and writing – review & editing; I. H.: investigation, data curation, and writing – review & editing; T. W.: investigation, data curation, and writing – review & editing; F. W.: investigation, data curation, and writing – review & editing; J. H.: investigation, data curation, and writing – review & editing; R. W.: investigation, data curation, and writing – review & editing; A. M. G.: conceptualization, investigation, data curation, and writing – review & editing; G. G.: investigation, data curation, and writing – review & editing; G. K.: investigation, data curation, and writing – review & editing; G. T.: resources, supervision, funding acquisition, and writing – review & editing; S. A. H.: conceptualization, data curation, supervision, and review & editing; and T. R.: conceptualization, formal analysis, funding acquisition, project administration, supervision, writing – original draft, and writing – review & editing.

## Conflicts of interest

There are no conflicts to declare.

## Data availability

All evaluated data are available in the manuscript. The data supporting this article are included as part of the supplementary information (SI). Supplementary information is available. See DOI: https://doi.org/10.1039/d5tc02554k.

Additional information/data can be obtained upon reasonable request.

## Acknowledgements

The authors gratefully acknowledge Graz University of Technology for financing this work through the Lead Project Porous Materials@Work for Sustainability (LP-03). S. A. H. gratefully acknowledges funding from the Engineering and Physical Sciences Research Council (EPSRC, EP/X012344/1). This work used the ARCHER2 UK National Supercomputing Service (https://www.archer2.ac.uk) *via* our membership of the UK's HEC Materials Chemistry Consortium, which is funded by EPSRC (EP/L000202).

## References

1 H. Park, S. Kumar R, A. Akande, S. Sanvito and F. El-Mellouhi, *Int. J. Hydrogen Energy*, 2022, **47**, 3358–3370.
2 Y.-Y. Sun, M. L. Agiorgousis, P. Zhang and S. Zhang, *Nano Lett.*, 2015, **15**, 581–585.
3 R. Zhou, X. Liu, S. Zhang, L. Liu, L. Wan, H. Guo, X. Yang, Z. Cheng, L. Hu, H. Niu and X. Mao, *Mater. Sci. Semicond. Process.*, 2021, **124**, 105613.
4 B. V. Gabrel'yan, A. A. Lavrentiev, I. Y. Nikiforov and V. V. Sobolev, *J. Struct. Chem.*, 2008, **49**, 788–794.
5 L. Yu, J. Li, G. Wang, B. Peng, R. Liu, L. Shi and G. Zhang, *ACS Appl. Mater. Interfaces*, 2021, **13**, 61116–61128.
6 Y. Bai, Z. H. J. Khoo, R. I. Made, H. Xie, C. Y. J. Lim, A. D. Handoko, V. Chellappan, J. J. Cheng, F. Wei, Y.-F. Lim and K. Hippalgaonkar, *Adv. Mater.*, 2024, **36**, e2304269.
7 A. Sarilmaz, E. Genc, E. Aslan, A. Ozen, G. Yanalak, F. Ozel and I. H. Patir, *J. Photochem. Photobiol., A*, 2020, **400**, 112706.
8 W. Wang, Q. Sheng, G. Zhi, Y. Zhao, R. Qu, L. Sun and S. Zhang, *Appl. Surf. Sci.*, 2023, **639**, 158251.
9 S. Kumar R, A. Akande, F. El-Mellouhi, H. Park and S. Sanvito, *Phys. Rev. Mater.*, 2020, **4**, 75401.
10 T. Rath, J. M. Marin-Beloqui, X. Bai, A.-C. Knall, M. Sigl, F. G. Warchomicka, T. Griesser, H. Amenitsch and S. A. Haque, *ACS Appl. Mater. Interfaces*, 2023, **15**, 41624–41633.
11 J. Lee, H. Kim, T. Lee, W. Jang, K. H. Lee and A. Soon, *Chem. Mater.*, 2019, **31**, 9148–9155.
12 T. Zhang, T. Wang, F. Meng, M. Yang and S. Kawi, *J. Mater. Chem. C*, 2022, **10**, 5400–5424.
13 C. Buchmaier, T. Rath, F. Pirolt, A.-C. Knall, P. Kaschnitz, O. Glatter, K. Wewerka, F. Hofer, B. Kunert, K. Krenn and G. Trimmel, *RSC Adv.*, 2016, **6**, 106120–106129.
14 I. Zumeta-Dubé, J.-L. Ortiz-Quiñonez, D. Díaz, C. Trallero-Giner and V.-F. Ruiz-Ruiz, *J. Phys. Chem. C*, 2014, **118**, 30244–30252.
15 T. Fazal, B. Ismail, M. Shah, S. Iqbal, E. B. Elkaeed, N. S. Awwad and H. A. Ibrahium, *Sustainability*, 2022, **14**, 4603.
16 S. Akhil and R. G. Balakrishna, *J. Mater. Chem. A*, 2022, **10**, 8615–8625.
17 Y. Wang, S. R. Kavanagh, I. Burgués-Ceballos, A. Walsh, D. O. Scanlon and G. Konstantatos, *Nat. Photon.*, 2022, **16**, 235–241.
18 T. Fazal, S. Iqbal, M. Shah, A. Bahadur, B. Ismail, H. S. M. Abd-Rabboh, R. Hameed, Q. Mahmood, A. Ibrar, M. S. Nasar, Y. Ehsan, A. N. Shah Saqib, Adnan and M. A. Qayyum, *J. Mater. Sci.: Mater. Electron.*, 2022, **33**, 42–53.
19 N. Suriyawong, B. Aragaw, J.-B. Shi and M.-W. Lee, *J. Colloid Interface Sci.*, 2016, **473**, 60–65.
20 S. Moon, J. Park, H. Lee, J. W. Yang, J. Yun, Y. S. Park, J. Lee, H. Im, H. W. Jang, W. Yang and J. Moon, *Adv. Sci.*, 2023, **10**, 2206286.
21 C. Chen, M. Yasugi, L. Yu, Z. Teng and T. Ohno, *Appl. Catal., B*, 2022, **307**, 121152.
22 C. Chen, Z. Teng, M. Yasugi, H. Yang, Y. Cao, L. Yu and T. Ohno, *Mater. Lett.*, 2022, **325**, 132801.
23 T. J. McCarthy, T. A. Tanzer and M. G. Kanatzidis, *J. Am. Chem. Soc.*, 1995, **117**, 1294–1301.
24 R. McClain, C. D. Malliakas, J. Shen, J. He, C. Wolverton, G. B. González and M. G. Kanatzidis, *Chem. Sci.*, 2021, **12**, 1378–1391.
25 O. Glemser and M. Filcek, *Z. Anorg. Allg. Chem.*, 1955, **279**, 321–323.

 

26 C. Yang, Z. Wang, Y. Wu, Y. Lv, B. Zhou and W.-H. Zhang, *ACS Appl. Energy Mater.*, 2019, **2**, 182–186.
27 J. W. Boon, *Recl. Trav. Chim. Pays-Bas*, 1944, **63**, 32–34.
28 K. Qu, H. Bale, Z. W. Riedel, J. Park, L. Yin, A. Schleife and D. P. Shoemaker, *Cryst. Growth Des.*, 2022, **22**, 3228–3234.
29 E. Vakalopoulou, D. Knez, M. Sigl, G. Kothleitner, G. Trimmel and T. Rath, *ChemNanoMat*, 2023, **9**, e202200414.
30 P. D. McNaughter, S. A. Saah, M. Akhtar, K. Abdulwahab, M. A. Malik, J. Raftery, J. A. M. Awudza and P. O'Brien, *Dalton Trans.*, 2016, **45**, 16345.
31 M. Al-Shakban, P. D. Matthews and P. O'Brien, *Chem. Commun.*, 2017, **53**, 10058–10061.
32 M. D. Khan, M. A. Malik, J. Akhtar, S. Mlowe and N. Revaprasadu, *Thin Solid Films*, 2017, **638**, 338–344.
33 P. S. Nair, T. Radhakrishnan, N. Revaprasadu, G. Kolawole and P. O'Brien, *J. Mater. Chem.*, 2002, **12**, 2722–2725.
34 T. Rath, M. Edler, W. Haas, A. Fischereder, S. Moscher, A. Schenk, R. Trattnig, M. Sezen, G. Mauthner, A. Pein, D. Meischler, K. Bartl, R. Saf, N. Bansal, S. A. Haque, F. Hofer, E. J. W. List and G. Trimmel, *Adv. Energy Mater.*, 2011, **1**, 1046–1050.
35 E. Vakalopoulou, T. Rath, M. Kräuter, A. Torvisco, R. C. Fischer, B. Kunert, R. Resel, H. Schröttner, A. M. Coclite, H. Amenitsch and G. Trimmel, *ACS Appl. Nano Mater.*, 2022, **5**, 1508–1520.
36 E. Vakalopoulou, T. Rath, F. G. Warchomicka, F. Carraro, P. Falcaro, H. Amenitsch and G. Trimmel, *Mater. Adv.*, 2022, **3**, 2884–2895.
37 A. J. MacLachlan, F. T. F. O'Mahony, A. L. Sudlow, M. S. Hill, K. C. Molloy, J. Nelson and S. A. Haque, *Chem. Phys. Chem.*, 2014, **15**, 1019–1023.
38 F. T. F. O'Mahony, U. B. Cappel, N. Tokmoldin, T. Lutz, R. Lindblad, H. Rensmo and S. A. Haque, *Angew. Chem. Int. Ed.*, 2013, **52**, 12047–12051.
39 S. Dowland, T. Lutz, A. Ward, S. P. King, A. Sudlow, M. S. Hill, K. C. Molloy and S. A. Haque, *Adv. Mater.*, 2011, **23**, 2739–2744.
40 T. Lutz, A. MacLachlan, A. Sudlow, J. Nelson, M. S. Hill, K. C. Molloy and S. A. Haque, *Phys. Chem. Chem. Phys.*, 2012, **14**, 16192–16196.
41 K. Momma and F. Izumi, *J. Appl. Crystallogr.*, 2011, **44**, 1272–1276.
42 V. Kupčík and L. Veselá-Nováková, *TMPM, Tschermaks Mineral. Petrogr. Mitt.*, 1970, **14**, 55–59.
43 V. Darji, P. Desai, M. P. Deshpande, S. Chaki, V. Sathe, B. S. Bhatt and R. A. Dabhi, *Mater. Chem. Phys.*, 2023, **295**, 127049.
44 Y. Zhao, K. T. E. Chua, C. K. Gan, J. Zhang, B. Peng, Z. Peng and Q. Xiong, *Phys. Rev. B: Condens. Matter Mater. Phys.*, 2011, **84**, 205330.
45 J. Barthel, *Ultramicroscopy*, 2018, **193**, 1–11.
46 P. Kubelka and F. Munk, *Z. Tech. Phys.*, 1931, **12**, 593–601.
47 P. Makuła, M. Pacia and W. Macyk, *J. Phys. Chem. Lett.*, 2018, **9**, 6814–6817.
48 T. Wada and T. Maeda, *Phys. Status Solidi C*, 2017, **14**, 1600196.
49 R. S. Silva, H. D. Mikhail, E. V. Guimarães, E. R. Gonçalves, N. F. Cano and N. O. Dantas, *Molecules*, 2017, **22**, 1142.
50 V. Kaltenhauser, T. Rath, W. Haas, A. Torvisco, S. K. Müller, B. Friedel, B. Kunert, R. Saf, F. Hofer and G. Trimmel, *J. Mater. Chem. C*, 2013, **1**, 7825.
51 X. Wang, A. M. Ganose, S. R. Kavanagh and A. Walsh, *ACS Energy Lett.*, 2022, **7**, 2954–2960.
52 A. K. Jena, A. Kulkarni and T. Miyasaka, *Chem. Rev.*, 2019, **119**, 3036–3103.
53 K. Makino, H. Imaishi, S. Morinishi, T. Takeuchi and Y. Fujiza, *Biochem. Biophys. Res. Commun.*, 1986, **141**, 381–386.
54 E. Finkelstein, G. M. Rosen and E. J. Rauckman, *Arch. Biochem. Biophys.*, 1980, **200**, 1–16.
55 E. Finkelstein, G. M. Rosen and E. J. Rauckman, *J. Am. Chem. Soc.*, 1980, **102**, 4994–4999.
56 F. Parrino, S. Livraghi, E. Giamello, R. Ceccato and L. Palmisano, *ACS Catal.*, 2020, **10**, 7922–7931.
57 D. T. Sawyer, M. J. Gibian, M. M. Morrison and E. T. Seo, *J. Am. Chem. Soc.*, 1978, **100**, 627–628.
58 T. Shoji, L. Li, Y. Abe, M. Ogata, Y. Ishimoto, R. Gonda, T. Mashino, M. Mochizuki, M. Uemoto and N. Miyata, *Anal. Sci.*, 2007, **23**, 219–221.
59 S. Fuloria, V. Subramaniyan, S. Karupiah, U. Kumari, K. Sathasivam, D. U. Meenakshi, Y. S. Wu, M. Sekar, N. Chitranshi, R. Malviya, K. Sudhakar, S. Bajaj and N. K. Fuloria, *Antioxidants*, 2021, **10**, 128.
60 R. J. E. Westbrook, T. J. Macdonald, W. Xu, L. Lanzetta, J. M. Marin-Beloqui, T. M. Clarke and S. A. Haque, *J. Am. Chem. Soc.*, 2021, **143**, 12230–12243.
61 N. Aristidou, C. Eames, M. S. Islam and S. A. Haque, *J. Mater. Chem. A*, 2017, **5**, 25469–25475.
62 T. Webb, X. Liu, R. J. Westbrook, S. Kern, M. T. Sajjad, S. Jenatsch, K. D. G. I. Jayawardena, W. H. K. Perera, I. P. Marko, S. Sathasivam, B. Li, M. Yavari, D. J. Scurr, M. R. Alexander, T. J. Macdonald, S. A. Haque, S. J. Sweeney and W. Zhang, *Adv. Energy Mater.*, 2022, **12**, 2200666.
63 J. Guo, B. Wang, D. Lu, T. Wang, T. Liu, R. Wang, X. Dong, T. Zhou, N. Zheng, Q. Fu, Z. Xie, X. Wan, G. Xing, Y. Chen and Y. Liu, *Adv. Mater.*, 2023, **35**, e2212126.
64 G. Kresse and D. Joubert, *Phys. Rev. B: Condens. Matter Mater. Phys.*, 1999, **59**, 1758–1775.
65 A. V. Krukau, O. A. Vydrov, A. F. Izmaylov and G. E. Scuseria, *J. Chem. Phys.*, 2006, **125**, 224106.
66 J. Heyd, G. E. Scuseria and M. Ernzerhof, *J. Chem. Phys.*, 2003, **118**, 8207–8215.
67 M. Ångqvist, W. A. Muñoz, J. M. Rahm, E. Fransson, C. Durniak, P. Rozyczko, T. H. Rod and P. Erhart, *Adv. Theory Simul.*, 2019, **2**, 1900015.
68 A. Zunger, S.-H. Wei, L. G. Ferreira and J. E. Bernard, *Phys. Rev. Lett.*, 1990, **65**, 353–356.
69 A. M. Ganose, A. J. Jackson and D. O. Scanlon, *J. Open Source Softw.*, 2018, **3**, 717.
70 B. Zhu, S. R. Kavanagh and D. Scanlon, *J. Open Source Softw.*, 2024, **9**, 5974.
71 K. Brlec, D. Davies and D. Scanlon, *J. Open Source Softw.*, 2021, **6**, 3171.